

Accepted Manuscript

Full length article

Improving our understanding of metal implant failures: Multiscale chemical imaging of exogenous metals in *ex-vivo* biological tissues

Alexander P. Morrell, Hayley Floyd, J. Frederick W. Mosselmans, Liam M. Grover, Hiram Castillo-Michel, Edward Davis, Julia E. Parker, Richard A. Martin, Owen Addison

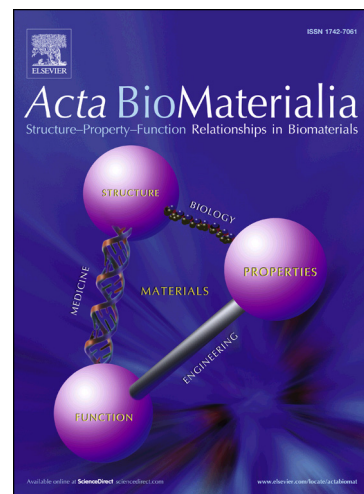
PII: S1742-7061(19)30398-8
DOI: <https://doi.org/10.1016/j.actbio.2019.05.071>
Reference: ACTBIO 6172

To appear in: *Acta Biomaterialia*

Received Date: 10 January 2019
Revised Date: 23 May 2019
Accepted Date: 28 May 2019

Please cite this article as: Morrell, A.P., Floyd, H., W. Mosselmans, J.F., Grover, L.M., Castillo-Michel, H., Davis, E., Parker, J.E., Martin, R.A., Addison, O., Improving our understanding of metal implant failures: Multiscale chemical imaging of exogenous metals in *ex-vivo* biological tissues, *Acta Biomaterialia* (2019), doi: <https://doi.org/10.1016/j.actbio.2019.05.071>

This is a PDF file of an unedited manuscript that has been accepted for publication. As a service to our customers we are providing this early version of the manuscript. The manuscript will undergo copyediting, typesetting, and review of the resulting proof before it is published in its final form. Please note that during the production process errors may be discovered which could affect the content, and all legal disclaimers that apply to the journal pertain.



Article type: Full Paper Direct Submission

Improving our understanding of metal implant failures: Multiscale chemical imaging of exogenous metals in *ex-vivo* biological tissues.

Alexander P. Morrell^a, Hayley Floyd^b, J. Frederick W. Mosselmans^c, Liam M. Grover^b, Hiram Castillo-Michel^d, Edward Davis^e, Julia E. Parker^c, Richard A. Martin^{a*} and Owen Addison^{b,*}.

^a University of Aston, Birmingham, B4 7ET, UK.

^b University of Birmingham, Birmingham, B15 2TT, UK.

^c Diamond Light Source, Didcot, OX11 0DE, UK.

^d European Synchrotron Radiation Facility, Grenoble, Cedex 9, France.

^e University Hospitals Birmingham, Birmingham, B15 2TH, UK.

^f University of Alberta, Edmonton, AB T6G, Canada.

*Co-last author and corresponding author

Corresponding author(s): Owen Addison,
Faculty of Medicine and Dentistry,
University of Alberta,
Edmonton,
Canada.

Telephone: +1 780 492 5308
E-Mail: oaddison@ualberta.ca

Richard Martin,
School of Engineering & Applied Science and Aston Institute of
Materials Research,
University of Aston,
Birmingham,
United Kingdom.

Telephone: +44 (0)121 204 5111
E-Mail: r.a.martin@aston.ac.uk

Keywords: XANES mapping, metal particle chemistry, microfocus spectroscopy, XRF, CoCr chemistry, total hip replacement.

ABSTRACT

Biological exposures to micro- and nano-scale exogenous metal particles generated as a consequence of in-service degradation of orthopaedic prosthetics can result in severe adverse tissues reactions. However, individual reactions are highly variable and are not easily predicted, due to in part a lack of understanding of the speciation of the metal-stimuli which dictates cellular interactions and toxicity. Investigating the chemistry of implant derived metallic particles in biological tissue samples is complicated by small feature sizes, low concentrations and often a heterogeneous speciation and distribution. These challenges were addressed by developing a multi-scale two-dimensional X-ray absorption spectroscopic (XAS) mapping approach to discriminate sub-micron changes in particulate chemistry within *ex-vivo* tissues associated with failed CoCrMo total hip replacements (THR). As a result, in the context of THR, we demonstrate much greater variation in Cr chemistry within tissues compared with previous reports. Cr compounds including phosphate, hydroxide, oxide, metal and organic complexes were observed and correlated with Co and Mo distributions. This variability may help explain the lack of agreement between biological responses observed in experimental exposure models and clinical outcomes. The multi-scale 2D XAS mapping approach presents an essential tool in discriminating the chemistry in dilute biological systems where speciation heterogeneity is expected.

1. INTRODUCTION

The presence of exogenous metallic microparticles, nanoparticles, complexes and ions in biological systems is of great interest to human health. Exposures may be inadvertent, through ingestion, inhalation or surface absorption routes. [1-3] Alternatively, metal-species may be introduced for therapeutic, diagnostic or cosmetic applications, or generated *in-situ* as a result of the degradation of an implanted prosthesis or device. [4-6] The biological significance of an exposure is dictated by both the physico-chemical nature of the metal, the location of the exposure and by the host organism's physiological response, which will differ between individual subjects. [3, 7] Factors influencing biological reactivity include the size, [8, 9] morphology, [10, 11] composition, [12] solubility, [3] surface charge and distribution of metallic particles [13, 14] and the local concentration and binding affinity of ions. [15] The chemical species in which an exogenous metal presents, and its stability within a specific physiological environment dictates many of these factors and therefore influences the biological outcome. An exposure route of increasing significance to healthcare, is the degradation of metal implant surfaces leading to the *in-situ* release of micro- and nano-sized metal particles and soluble ions. [10, 16] In particular, the release of metallic implant derivatives from orthopaedic total joint replacements has been associated with osteolytic activity and implant loosening. [17-20] A lack of understanding of the complex nature of the metal-species formed, and how these species may be further transformed within biological media, has prevented the translation of findings from *in-vitro* biological modelling efforts, into informed clinical monitoring and assessment of individual risk. In this work, a novel multi-scale chemical imaging approach is applied to tissues associated with failing total-hip-replacement (THR), shedding light on the hereto unreported heterogeneity in speciation of the micron and nano-sized debris formed.

Many studies have attempted to correlate concentrations of exogenous elements in tissues and fluids with a biological response. However, subtle variability in metal speciation may be a significant confounder when interpreting these data. For example, certain endogenous complexes of trivalent Cr (Cr(III)) are involved in glucose metabolism, however hexavalent Cr (Cr(VI)) is a group 1 carcinogen. [21, 22] Similarly, different Nickel (II) salts, Co compounds and structural polymorphs of Titanium dioxide, detected in biological systems, demonstrate significant differences in cellular cytotoxicity and genotoxicity. [21, 23-26] To fully understand the implications of an exposure, the local chemistry of the metals directly involved in the biological interactions must be known. Characterisation is complicated by the dynamic nature of biomolecules adsorbing to particles resulting in complexes which change depending on their local environment. [27] This highlights the importance of maintaining an appropriate environment during characterisation in order to preserve the *in-situ* chemical form.

The chemistry of small particles at the micron and nanometric scale is especially difficult to identify as most characterisation techniques routinely applied to *ex-vivo* tissue analysis, provide bulk chemical information failing to distinguish differences between the particle core and surface. In addition, these particles are often found as nano- or micro- sized agglomerates at trace levels heterogeneously distributed throughout the sample. [28, 29] Therefore the analytical technique must provide adequate detection limits, with a high spatial resolution, and be able to interrogate the composition and chemistry over a relevant field of view in a non-destructive manner. Diffraction based methods do not possess the required sensitivities to interrogate these types of systems, and mass spectrometry techniques are destructive and lack sufficient spatial resolution. [30] Samples for electron microprobes must be dehydrated, which may influence the natural chemical form and typically have severely restricted fields of view with lower

sensitivities in comparison to other interrogation sources. ^[31] Proton or particle probes can be utilized to investigate the chemical composition using Particle Induced X-ray Emission (PIXE). ^[32] However, X-ray sources can be used to map the elemental distribution (X-ray Fluorescence Spectroscopy) whilst giving an insight into the chemistry (X-ray Absorption Spectroscopy). ^[32, 33] High flux X-ray micro and nano probes are widely used to interrogate exogenous features within biological samples due to their detection limits, spatial resolution and flexibility of the sample environment which enables measurements to be conducted on dehydrated tissues and where required, on hydrated tissues under cryogenic conditions.

X-ray absorption near edge structure (XANES) can be used to determine the oxidation state, coordination number, covalence and the symmetry of the metal particles. ^[34] Conventional XANES methods interrogate the absorption coefficient by scanning through carefully selected X-ray energies at a single point within the sample. This has previously been used to identify different metallic species within tissues exposed to THR systems. ^[35, 36] Whilst these studies may show the predominate species present, what is often neglected is the full chemical variation present, due to the interrogation method. In samples where speciation heterogeneity on length scales smaller than the resolution of the X-ray beam are present, the resultant spectrum is a weight sum of these species. These may be difficult to segment in scenarios with several species with similar spectral features. To improve chemical identification a higher resolution source may be used. However, significant problems arise in XANES measurements when the X-ray beam size approximates the dimensions of the interrogated features. Subtle movements in the sample (due to local heating) or beam position (instability in the optics) results in the X-ray beam drifting off the feature, which in turn generates uninterpretable data. ^[37] This scenario is often the case when investigating metallic particles in biological tissues, as they contain many

isolated features which limits the available areas for spectroscopic analyses. A multi-scale XANES mapping approach can be used to reduce these associated limitations. [37, 38]

Recently the acquisition of fluorescence energy maps (XANES maps) has become prevalent on hard X-ray micro- and nano- probes to investigate the speciation of dilute elements spatially. XANES mapping involves mapping in three axes, two image axes and one energy. Conventionally, the energy is the outer axis whereby a series of XRF maps are recorded at specific energy values corresponding to the absorption edge of the target element. These are subsequently stacked to produce an individual spectrum for each pixel. Recently, Bosenberg *et al* used the energy as the inner axis to collect XANES images by using a QEXAFS monochromator. Whilst this has significantly advantages when investigating transient species, there is no straight forward method of correcting beam/sample drift. [39] This correction is essential when XANES mapping exogenous particles in soft tissues which are susceptible to movement. XANES mapping results in a chemical image containing spectroscopic information within a 2-dimensional field. This adds additional information regarding the chemistry of the system over a user defined area, which may be useful for co-locative studies. Isolated features which previously could not be identified spectroscopically can be investigated with the use of post-analytical stack alignments, which alleviate the effects caused by movement. [40]

It is hypothesized that conventional XANES methods at an inappropriate resolution, limits the number of species identifiable in *ex-vivo* tissues that once surrounded CoCrMo THR. By using a multi-scale XANES mapping approach it is anticipated that better speciation discrimination will be achieved, ultimately allowing for more accurate characterisation of local chemistry. To our knowledge here for the first time a multi-scale XANES mapping approach has been applied

to investigate the speciation of metallic debris within such tissues. By using this approach, the entire chemical variability was assessed on different length scales, enabling samples containing heterogeneous species to be better identified. In addition, isolated small features renowned for producing poor static XANES measurements were interrogated with the aid of post analytical alignment.

2. MATERIALS AND METHODS

Synovial sheath tissues were taken at the time of scheduled revision surgery of CoCrMo THRs from two consenting patients who exhibited similar device histories, implant bearing surfaces (metal-on-metal), and alloy composition (ASTM grades F75 and F799 (58.9 - 69.5% Co, 27.0 - 30.0% Cr, 5.0 - 7.0% Mo)).^[41] The patients underwent revision of a CoCr R3 Acetabular cup Synergy Hip stem combination (*Smith and Nephew, UK*), and a Birmingham Hip Resurfacing (*Smith and Nephew, UK*) after 6.5 and 6 years, respectively. For both patients the reason for revision was a prosthesis associated joint effusion with elevated systemic implant ion levels. Retrieved tissue explants were orientated, immediately placed on dry ice for transfer and then stored at -80°C at a Human Biomaterials Resource Centre approved site at the University of Birmingham (ethical approval REC 09/H1010/75). Serial frozen tissue sections between 4-8 µm in thickness were prepared using a cryotome with a tungsten carbide blade. Sections were mounted on silicon nitride membranes (*Silson Ltd, UK*) or Ultralene (*SPEX®SamplePrep, USA*). Tissues were interrogated at the following beamlines: I18 (microfocus spectroscopy beamline) and I14 (hard X-ray Nanoprobe), Diamond Light Source (*Harwell Science and Innovation Campus, UK*). ID21 (X-ray microscope beamline), European Synchrotron Radiation Facility (*Grenoble, France*). X05LA (MicroXAS beamline), Swiss Light source (*Villigen, Switzerland*). I18 utilises a Kirkpatrick-Baez (KB) mirror system to focus the beam into the micron range and uses a liquid nitrogen cooled Si(111) monochromator to cycle through the

required energies. [42, 43] X-ray fluorescence maps were produced using an incident energy of 8.5 keV, which allowed detection of elements Co down to Cl. Samples were mounted onto Ultralene and positioned 45° to the incident source. With the mounting angle taken into consideration the beam was focused down to a foot-print size of 3 x 3 µm. An acquisition time of 200 ms per pixel was used, and the signal was acquired with a 4-element Vortex Si drift detector (*Hitachi Hi-Technologies Science, Tokyo*). A step size of 3 µm was used for both horizontal and vertical movement. Measurements were undertaken at room temperature. Two large XRF maps were acquired on a single tissue section, both of which had similar implant-related metal distributions. A total of 91 sequential energy points were chosen to produce XANES maps (Supplementary Table 1). To interrogate at a higher resolution, the tissues were mounted onto Silicon Nitride membranes and taken to the scanning X-ray microscope end-station on ID21 at the European Synchrotron Radiation Facility (*Grenoble, France*). [44] ID21 uses a fixed exit double crystal Si(111) monochromator to select and scan the energy of the beam. This is then focused using a KB mirror system. Measurements are made using an energy dispersive detector; a silicon drift diode (*SGX Sensortech, Switzerland*). Measurements were undertaken at room temperature under a vacuum. The X-ray beam was focused to a footprint of 600 x 300 nm (H x V) and an incident energy of 7.8 keV was used to allow detection of Co and Cr. An acquisition time of 100 ms was used per pixel. A second energy of 6 keV was utilized to re-measure the same area to generate a better signal-to-noise ratio on low Z-elements found in tissues. This energy was chosen to still allow detection of Cr to assess whether an image shift had occurred, as changing the monochromator Bragg angle may have caused a movement of the beam position. No shift in the Cr signals was detected and as a result no alignment was necessary between the 7.8 and 6 keV maps. Samples were mounted on Silicon Nitride membranes and imaged in vacuum. A total of 11 (83 x 83 µm) XRF maps were

generated by imaging three tissue serial sections for matched patient tissues interrogated at I18. To produce fluorescence XANES maps a total of 117 sequential energy points were chosen, the energy values can be found in Supplementary Table 1.

To detect the presence of Mo, the tissues were taken to the MicroXAS beamline at the Swiss Light Source (*Villigen, Switzerland*). Similar to I18 a KB mirror system was utilized to focus the X-ray beam to a footprint of $1 \times 1 \mu\text{m}$. An incident energy of 20.5 keV allowed the detection of Molybdenum. An acquisition time of 5 s per pixel was used to generate adequate statistics, and a multi-element Si solid state detector (*Ketek, Germany*) was used to collect the fluorescence signal. The chemistry of both Co and Cr were interrogated at the hard X-ray nanoprobe I14 at Diamond Light Source. Samples were mounted onto Silicon Nitride membranes and an incident energy of 9.2 keV was selected using a horizontal double crystal monochromator. The X-ray beam was focused using a KB mirror system to a footprint of $250 \times 250 \text{ nm}$. XRF maps were acquired using a 4-element Si drift detector (*Rayspec, UK*) with an acquisition time of 100 ms per pixel. Measurements were undertaken at room temperature. A single fluorescence map, with resolution of $1 \mu\text{m}$, imaged on a serial section matched those imaged at I18 and ID21. Two higher resolution (250 nm) were subsequently imaged at regions of interest within the lower resolution map. Fluorescence XANES map were recorded for Co and Cr K-edge using 118 and 125 energy points respectively (Supplementary Table 1).

XRF maps collected from all beamlines were batch fitted using PyMCA. This software fits the fluorescent lines along with a background subtraction pixel by pixel.^[45] The fluorescent maps are shown as RGB images to allow clear visual co-locative representation of the metallic distribution throughout the tissue. Where the Co: Cr ratio map is shown in Figure 6b, the XRF

data was assessed semi-quantitatively. This was achieved by applying a matrix correction (based on a soft tissue composition) and considering excitation efficiencies calculated in PyMCAs inbuilt quantification algorithms. [45, 46]

The XANES map data were stacked, aligned and windowed at the emission energy of the element of interest (± 200 eV). Alignment was conducted using MANTiS for the data collected at Diamond Light Source and inhouse scripts, based on Python and PyMCA tools, was utilized for the data collected at the ESRF. [47, 48] Principle components (PCs) analysis and cluster analysis was undertaken on the XANES stacks. Before analysis each spectrum was normalized by dividing the intensity value by the last energy point. This is important as this eliminates PCs based on intensity rather than spectral differences. Clustered spectra were generated based on the PCs. The grouped spectra were normalized using software package ATHENA. [49] The spectra were compared against standards and linear combination fitting was attempted to reproduce the experimental data with combinations of standards. Linear regression analysis was used to cross-correlate XANES spectra acquired using different measurement approaches including comparison of point spectra, mapping spectra and spectra acquired at different spatial resolutions.

3. RESULTS AND DISCUSSION

3.1. Micro- XAFS/XRF measurements (3 μm resolution)

Ex-vivo peri-implant tissue was retrieved at the time of revision surgery from patients with CoCrMo THRs and was interrogated with μXRF and μXAFS . A representative μXRF image is shown in Figure 1a. The fluorescence intensity map shows an accumulation of Co and Cr following the tissue planes of the synovial sheath, with high intensity features of Co and Cr co-located surrounded by lower intensity regions of Cr. The co-location of Mo with high intensity Co and Cr identifies regions most closely matching the composition of the base metal

(Supplementary Figure 1). The distribution in fluorescence intensity of Co and Cr is consistent with previous reports.^[50] The quantitative values are summarised in Supplementary Table 2. Whilst the average concentration of Co and Cr within these tissues is similar to previous reports^[35, 36], the localised maximum concentrations are significantly higher. This heterogeneity in concentration is typically not detected by non-spatially resolved techniques such as mass spectrometry performed bulk on samples, but is essential to understand in the context of a biological response. A Cr K-edge XANES spectrum was recorded on a large feature possessing a high intensity signal, shown in Figure 1b. This area was selected to generate high quality data, a rationale adopted by many researchers.^[36, 51] However the selection method introduces bias sampling as the region with the highest intensity may not be representative speciation of the entire area. The spectrum shown in Figure 1b displays features characteristic of hydrated Cr phosphate (CrPO_4), which has been previously reported when adopting the same interrogation methods on similar tissues.^[35, 50] Undertaking spectroscopic measurements, mapping or point XANES, is undoubtedly limited by the intensity of the feature. In practice there must be a distinct detectable fluorescence peak above the noise limits to be constructed into a fluorescence XANES spectrum. Primarily, factors which influence this intensity are sample related (concentration of element of interest) and instrumental set-up (flux, solid angle, detector efficiency etc.). Regardless of employing a mapping or static measurement method, both are limited to the same detection limits. However, isolated features possessing adequate intensity often produce poor quality point measurements, due to movement related drawbacks as previously mentioned. A mapping approach can significantly improve the gathering of spectroscopic information on such features.

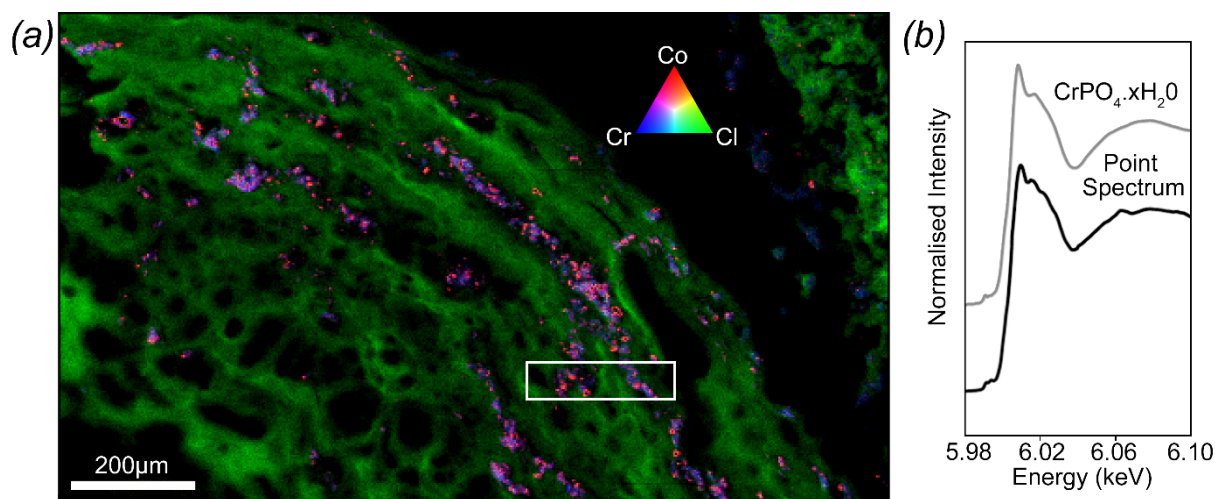


Figure 1. μ XRF and μ XANES analysis was undertaken at I18, *Diamond Light Source, UK*. **(a)** shows an XRF map of *ex-vivo* synovial sheath tissue, Cl (green) is a typical tissue marker and shows the geometry. Co and Cr (red and blue respectively) are co-located in areas but Cr appears more abundantly and in diffuse regions as well as single features. A point XANES measurement is shown in **(b)** which utilized a 3 μ m beam on a region with high Cr signal. The spectrum shows close resemblance to CrPO_4 (also shown in **b**).

XANES mapping reduced sampling bias, increased the size of the data set acquired and improved the quality of the spectroscopic data. A representative μ XANES map possessing regions of both high and low intensity Co and Cr fluorescence (250 x 50 μ m area taken from inset in Figure 1a) is shown in Figure 2. Principal component analysis identified four distinct spectra within the interrogated area (Figure 2). This method helps discriminate species present by summing pixels with similar spectral features, which is essential when investigating highly dilute samples. The high intensity regions (red) contained a larger contribution of metallic Cr than the surrounding regions, evident by the broader pre-peak at ~ 5995 eV. The surrounding clusters showed similar spectral features as the point XANES measurement shown in Figure 1. However, there were subtle difference at the post-edge peak, which were likely to be due to which Cr(III) species was present.

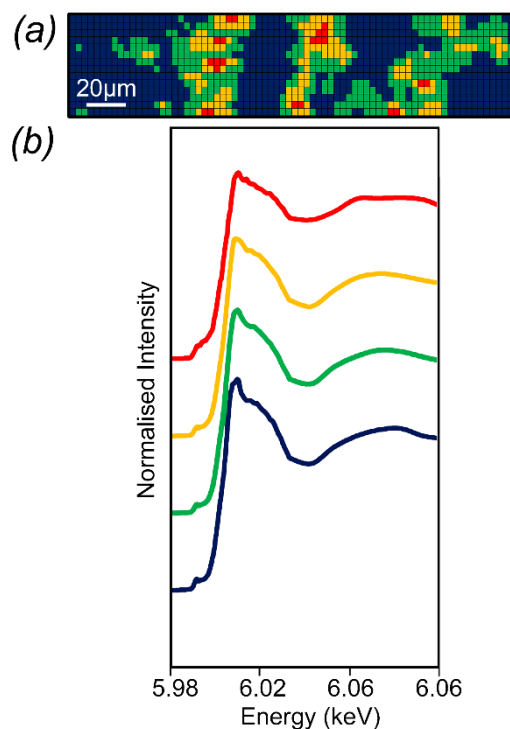


Figure 2. A 3 μm resolution beam was utilized to generate a $\sim 250 \times 50 \mu\text{m}$ XANES map. Each point was grouped based on spectral similarities into four clusters. The resulting cluster map is shown in (a). The resulting spectra are shown in (b).

3.2. Sub micron- XANES/ XRF (600 nm resolution)

Subsequent imaging on the same tissue was performed using a higher resolution source at ID21. Figure 3a shows that at this resolution, while high intensity regions of Co and Cr are still seen, in comparison with the μXRF shown previously, it is more evident that Cr is present in areas without the presence of a Co counterpart completely. Quantitative values are summarised in Supplementary Table 2. This shows clear variability in the ratio of Co: Cr signal at a submicron level. Whilst this does not confirm speciation variability it shows that the degradation mechanism of these implants and/or the biological/ physiological modification *in-situ*, can produce metal features with significantly different Co: Cr ratios in the surrounding tissues compared with the base alloy. Figure 3b shows the region which was subsequently XANES mapped, highlighted by an inset in Figure 3a. Radial selections starting from the centre of a high intensity particle, moving outwards were summed, and are indicated within Figure 3b. A clear decrease in the pre-peak is observed whilst moving away from the centre of high intensity

(Figure 3c and 3d), indicating a reduction in metallic fraction. This was confirmed using linear combination fitting (LCF) of metallic-CoCr and Cr(III) complexes, including $\text{Cr}(\text{OH})_3$, Cr_2O_3 and CrPO_4 as standards (Supplementary Figure 2). To help identify which Cr(III) complexes were present, PCA analysis was conducted and a set of 4 clusters were generated and grouped based on spectral similarities (Figure 4). The most abundant cluster (1) is best represented as a combination of CrPO_4 , $\text{Cr}(\text{OH})_3$ and metallic-CoCr. These species are the most widely reported and therefore it is not surprising that they are the most abundant when undertaking a spectroscopic mapping approach.^[35] Cluster 2 presents a difficult species to identify, a unique feature is observed at ~ 6025 eV which is present in all the contributing spectra. This feature cannot be explained from any of the organic Cr standards shown. Clusters 3 and 4 are also likely to be combinations of Cr(III) complexes with the highest fractions being Cr malate ($\text{C}_4\text{H}_4\text{CrO}_5$) and Cr acetate hydroxide ($\text{Cr}_3(\text{OH})_2(\text{OOCCH}_3)_7$), respectively. Regardless of the species observed, the spectral features of these components are significantly different from those seen when interrogating with a micron sized X-ray profile in a point spectrum fashion. To imitate the product of the high resolution XANES map recorded with a $3 \mu\text{m}$ resolution, a 5×5 -pixel area was summed (Figure 5). The summed and single point spectra, shown in Figure 1b, both contain the broadened pre-peak characteristic of CoCr, and similar edge and post peak regions suggesting primarily CrPO_4 content. The subtle intensity differences of the first interference peak between summed and single point spectra is likely to be due to dissimilar contributions from Cr(III) species at this location. Most importantly this shows that averaging over an area of heterogeneous speciation may not be an accurate representation of the species present. Supplementary Figures 3 and 4 summarize a statistical analysis of XANES spectra acquired using the different measurement approaches. Linear regression analyses applied to the Cr post-edge region (6.00 – 6.04 keV) on the high-resolution ID21 XANES map data (600 x 600 nm

per pixel), identified that only ~50% of spectra were well-represented by the 3x3 μm^2 average spectra of the entire measurement region ($R^2 > 0.9$, $p < 0.05$). Whilst XANES mapping at a 3 μm resolution (Figure 2) indicated potential variation in the spectra identified by PCA, linear regression comparing the most different components failed to discriminate significant differences. As over 1400 spectra were analysed in the I18 XANES map alone (Figure 2) and insignificant variation was observed, this emphasises that the measurement spatial resolution limits characterisation of Cr speciation in these samples.

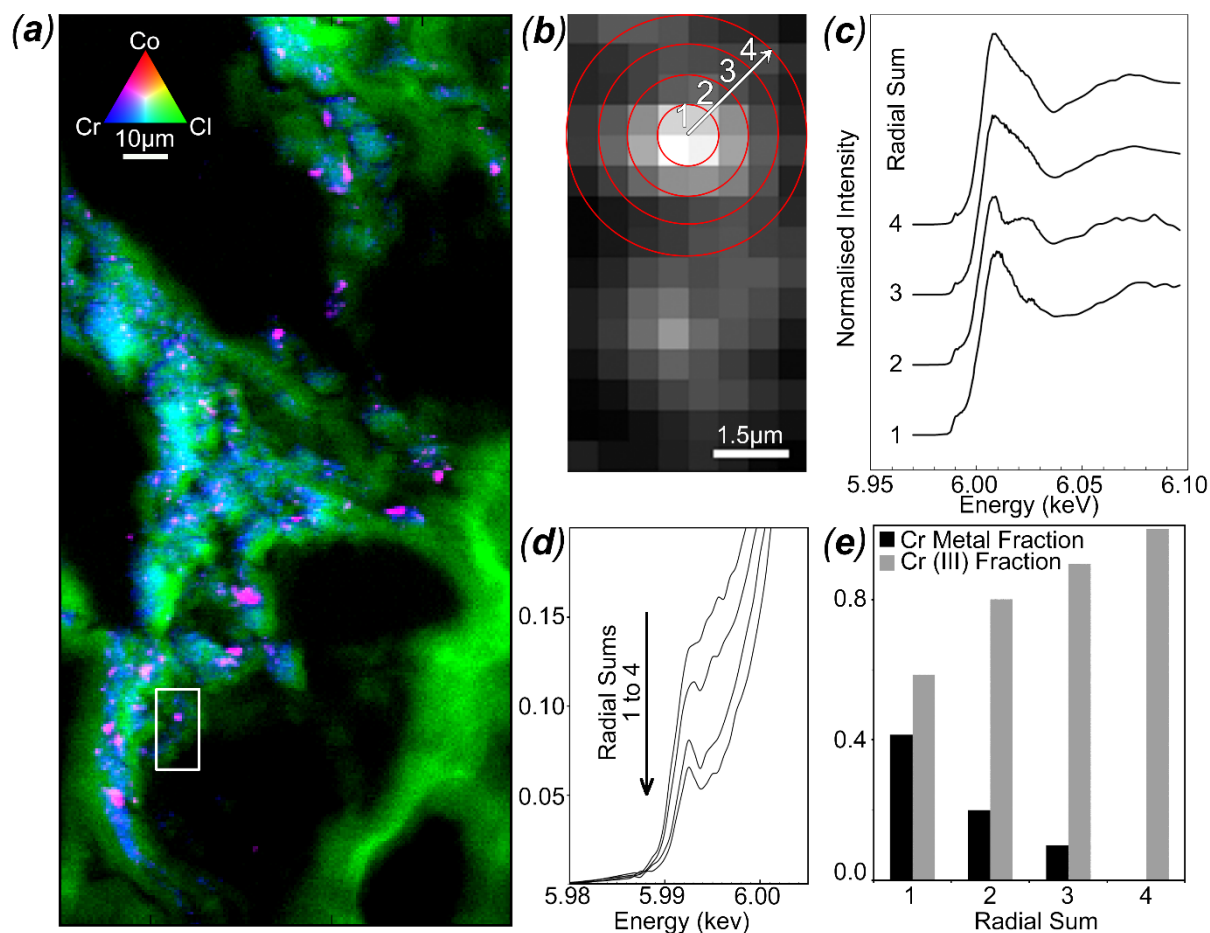


Figure 3. sub-micron-XRF and XANES mapping analysis undertaken on ID21. (a) shows a high resolution XRF map on the *ex-vivo* soft tissue (600 nm beam size). At this resolution it is more evident that CoCr features are present within a network of diffuse Cr. (b) shows an intensity map of the area subjected to Cr XANES mapping, highlighted by an inset in (a). To understand speciation variation across the high intensity CoCr regions, radial selections of the XANES spectra were taken, starting in the middle and moving outwards, the results are shown in (c). The pre-edge region, highlighted in (d), shows the further away from the centre of the feature causes a reduction in metallic fraction. (e) shows a histogram of how the metallic fraction reduces when moving away from the inside the core outwards (based off the pre-edge peak).

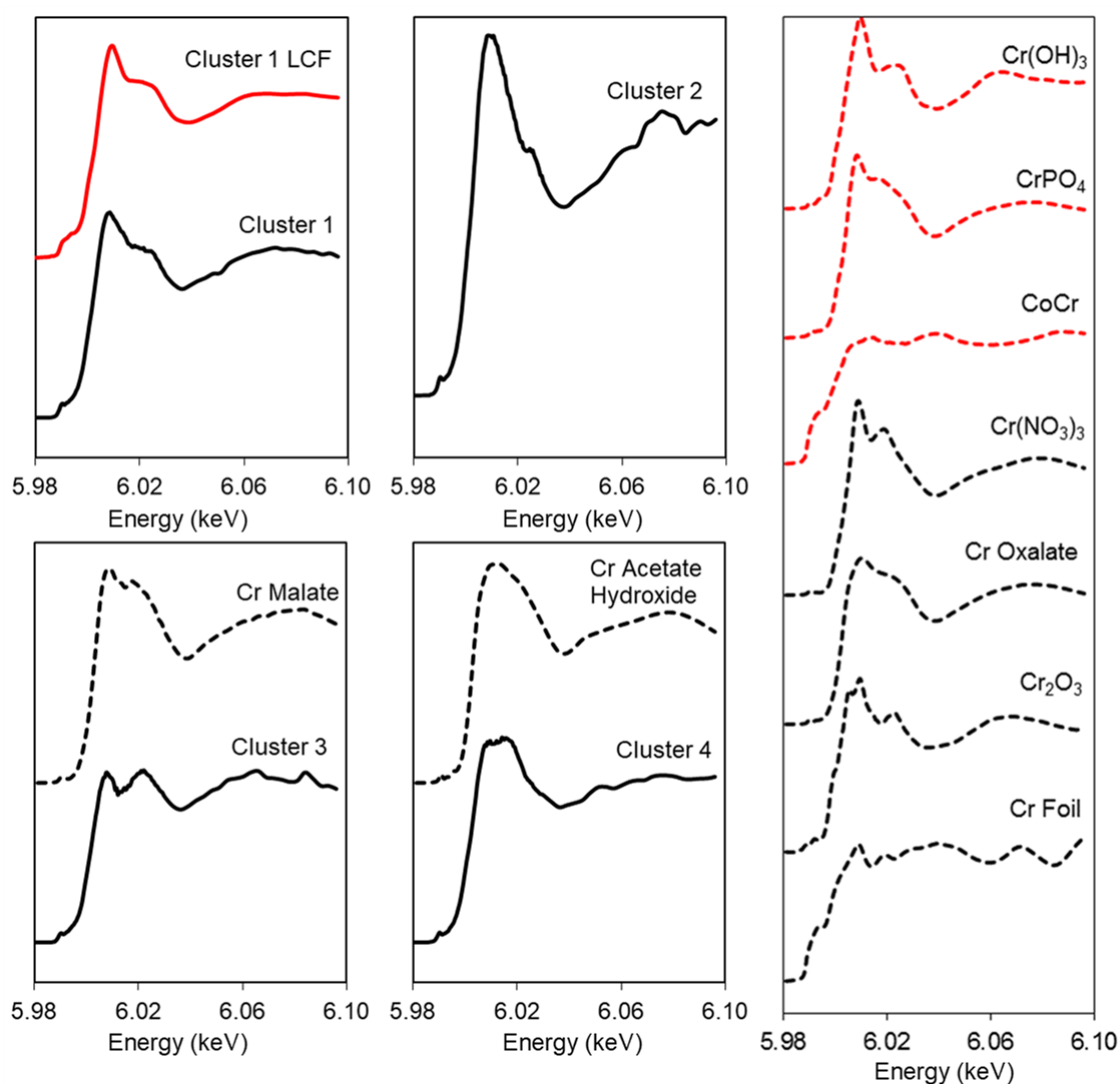


Figure 4. Shows the cluster analysis of the XANES mapping data in the region identified in Figure 3. XANES data was stacked and aligned using in-house ID21 algorithms. Six principle components were identified but only 4 clusters were used as after this point the spectra could be reproduced using linear combinations of standards in different ratios. Each cluster is shown on a separate graph (solid black line) and Cr standards which are thought to contribute to the spectra are shown (dashed-line). Cluster 1 is the most abundant spectra and from the linear combination fitting (LCF) it is likely to be a combination of CrPO_4 , Cr(OH)_3 and CoCr (34%, 41% and 25%, respectively). The spectrum in Cluster 2 contains a unique feature present at ~ 6025 eV which is not present in any of the organic or inorganic reference spectra. Cluster 3 and 4 are combinations of Cr complexes with CoCr , however a LCF is not shown as the predominate species present is Cr malate and acetate hydroxide, respectively.

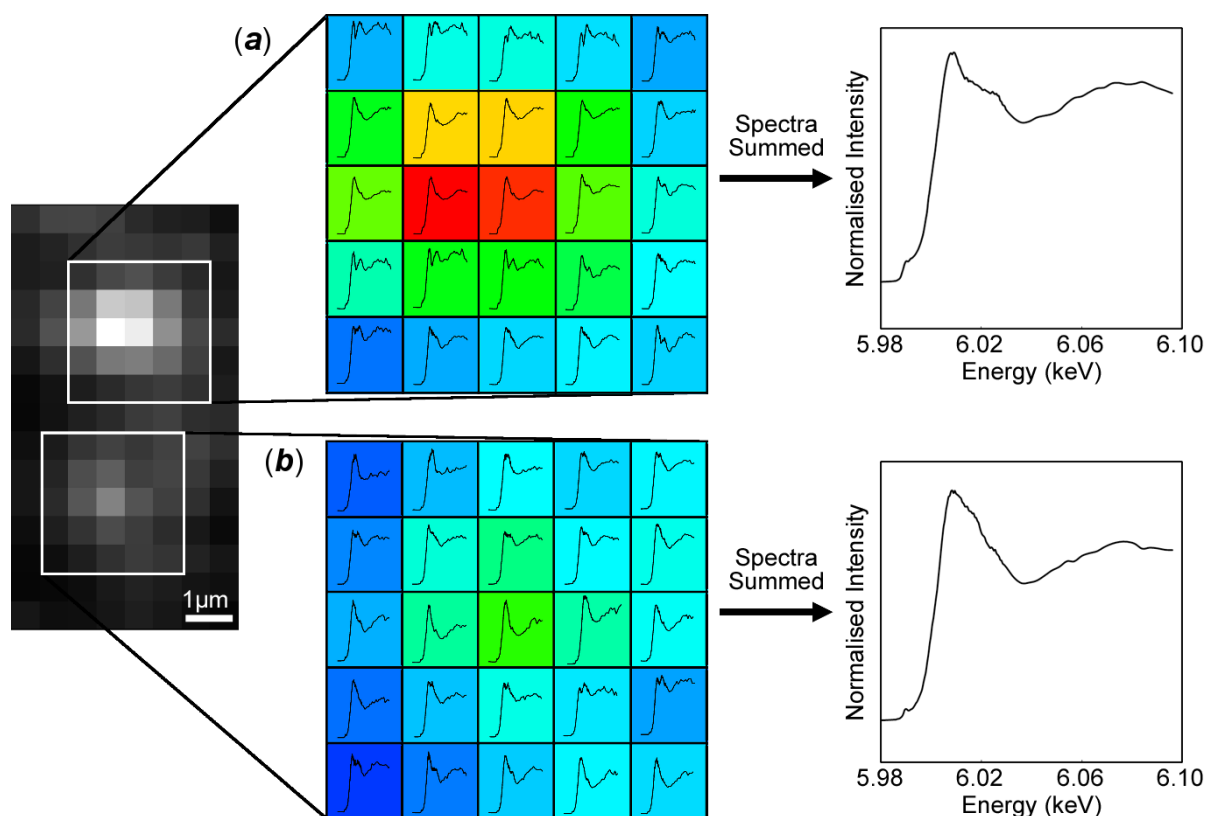


Figure 5. The two spectra shown on the right-hand side are a result of summing a $3 \times 3 \mu\text{m}$ area from the XANES map, mimicking a lower resolution static measurement. By averaging over a larger area some spectral features are lost which may be essential for working out which species are present. The top region results in a spectrum with prominent features similar to $\text{Cr}(\text{OH})_3$ and CrPO_4 complexes. The bottom region spectrum has a broader peak with no secondary peak, this feature is similar to those shown by organic Cr complexes.

3.3. Nano- XANES/ XRF (250 nm resolution)

XRF mapping, Co and Cr XANES were performed at the hard X-ray nanoprobe I14 (*Diamond Light Source, UK*), utilising a 250 nm X-ray beam.^[52] Interrogating Co with a XANES mapping approach reduces the likelihood of X-ray induced oxidation by significantly reducing the X-ray exposure time per pixel.^[53] The distribution of Co and Cr was similar to results recorded at ID21 (Figure 6a). A smaller region was subsequently imaged at 250 nm and the Co: Cr ratio was calculated (Figure 6b). To generate an accurate Co: Cr ratio map the data was considered in a semi-quantitative manner. The data outputted from XRF maps does not consider X-ray excitation efficiencies and sources of fluorescence attenuation throughout the sample. Deploying a semi-quantitative approach by accurately defining these parameters will enable

direct comparison of the relative element concentrations within a system. The exact concentration of each element cannot be reported without empirical calculation (with the use of calibration curves), utilising theoretical algorithms (with the use of reference materials) or using Monte-Carlo simulations.^[54-58] Generating ratios from the RAW data resulted in some pixels exceeding a ratio of 3: 1 (Co: Cr). Whereas applying a quantitative approach the same pixels reduced to less than 2: 1, this ratio is more representative of the base alloy. The effects of analysing semi-quantitatively are summarised in Supplementary Figure 5. Less than 0.1% of pixels containing both Co and Cr had a ratio similar to that of the bulk alloy.

To attempt to get a full representation of the Co speciation, an area containing both high and low Co: Cr were selected for XANES mapping. Pixels containing more Co than Cr were grouped into the 'high Co: Cr' category and vice versa for the 'low Co: Cr' category. In both cases, and when looking at each feature separately, the Co species present appeared metallic with no traces of oxide or organic complexes within the interrogated region. Previous reports on similar metallic exposures have shown both the presence of Co in a metallic form as well as a Co(II) structure.^[35, 59] In some of these previous cases the presence of an oxidized Co was attributed to the damaging effects of the beam exposure.^[35] A XANES mapping approach reduces the exposure time significantly. The XRF maps were recorded at 100 ms per pixel with 96 energy values, generating a total X-ray exposure time of 9.6 s per pixel spread across a time period > 2h. In contrast to previous reports, no Co oxide was seen in any of the XANES maps generated (equivalent of 7500 individual XANES spectra). The Cr species in areas with high Co: Cr contained a much larger fraction of metallic Cr (Figure 6d). Whereas in the Co deficient areas the pre-edge is lower, and a prominent secondary oscillation is present, characteristic of a Cr(III) complex such as the ones identified previously. Within this system there are features

that remain close to the original alloying composition and both Co and Cr XANES presented predominately metallic spectra. These findings indicate that high intensity regions of Co, Cr and Mo are likely to be in particulate form with predominately metallic chemistry appose to a soluble ionic species. However, there are regions where Cr features are Co deficient or even completely lacking a Co counterpart. This may be caused by dissolution of CoCr and reprecipitation locally as a stable Cr(III) complex, whilst Co is predominately observed as an ionic form and distributed systemically due to its increased solubility.^[60] This is supported by elevated Co levels (compared with Cr) in patient's urine and blood with similar metallic prosthetics.^[61, 62] The passive oxide surface of CoCr implant alloys consists largely of Cr₂O₃ however, this layer is typically 2-5 nm in thickness which cannot explain the metals features observed which are several microns in diameter.^[63, 64] Additionally, evidence collected from XANES demonstrates differences in chemistries expected to that of the native alloy. Irrespective of whether the metal derivatives are released from the bulk alloy, the surface oxide or modified to due corrosive mechanisms and/or biological/environmental processing, it is evident Co is deficient in most metal features observed within peri-implant tissues. The determining factor of whether Cr complexes or remains as a soluble ion is thought to be dependent on the local environment and availability of ligands and organic complexes. Whilst, the chemical form can be predicted based on relative elemental intensities, absorption spectroscopy is essential for validation of the exact speciation.

Understanding the chemistry of these metals is fundamental to understanding the mechanisms of their production and any associated processing upon leaving the implant surface. The speciation may also dictate the associated cellular behaviours, and thus be a contributing factor to the viability of the implant. Using more advanced spectroscopic techniques such as XANES mapping on these systems allows a larger area to be interrogated chemically, a higher number

of spectra to be recorded, improves the quality of data on isolated features, reduces the effects of beam exposure and generates a spatial aspect to the interpretation. By deploying a multi-scale approach, it is evident that resolution is a fundamental aspect in interrogating the speciation of heterogeneous samples. A compromise between a higher resolution (allowing a greater discrimination between heterogeneous species) and a lower resolution (enabling larger areas to be interrogated) must be achieved.

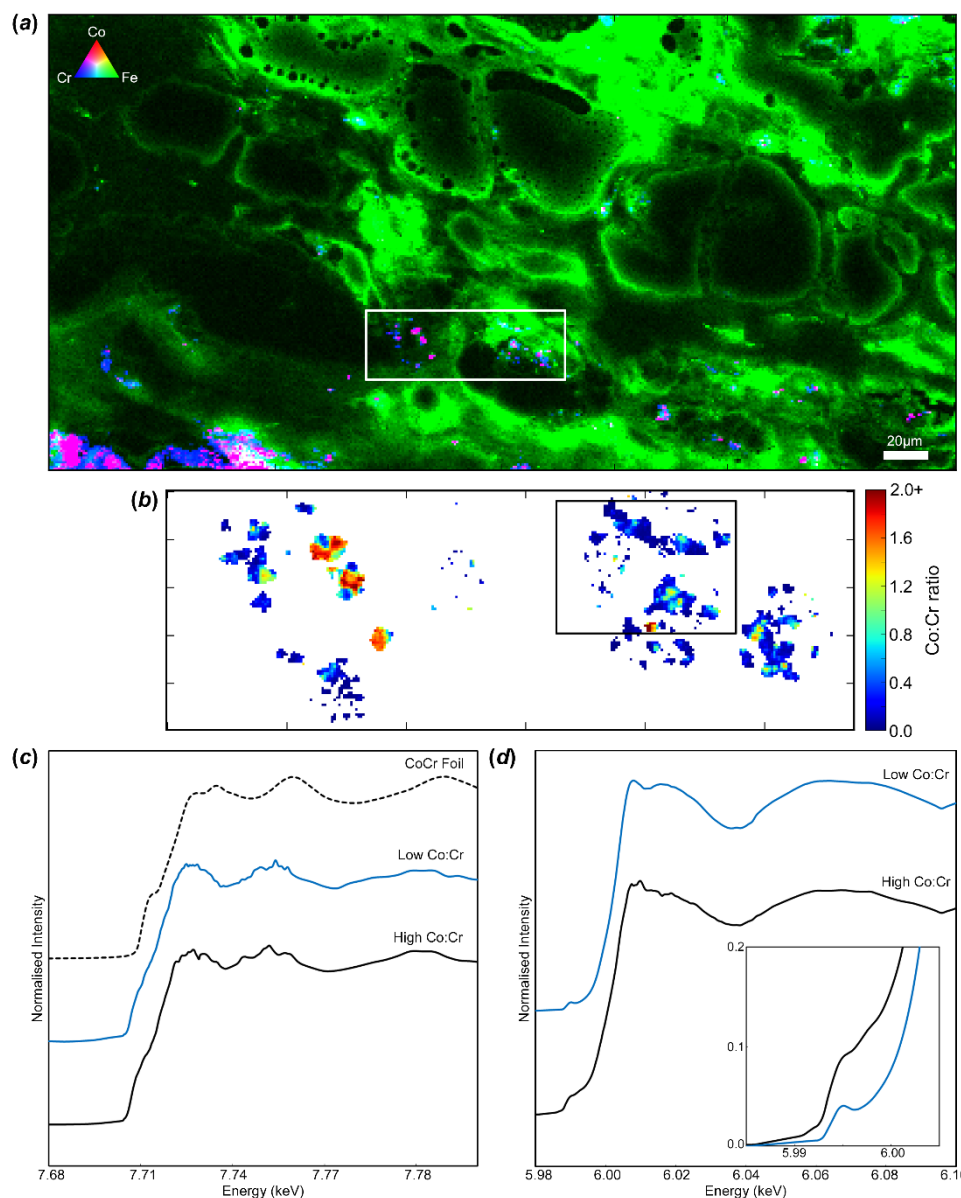


Figure 6. (a) XRF map of *ex-vivo* soft tissues recorded at the hard X-ray nano-probe I14. A step of 1 μm was used both horizontally and vertically. The elements shown are Co (red), Cr (blue) and Fe (green). Fe was utilised to observe the tissue geometry as it contained the highest signal-to-noise of all the soft tissue elements present. (b) Co: Cr ratio map from area highlighted in Figure 6a, a resolution of 250 nm was used. (c) Co and (d) Cr XANES spectra from the XANES map region highlighted in Figure 6b. The spectra shown are a result of summing spectra based on their Co: Cr ratios. Spectra containing high Co: Cr are shown in black, whereas spectra containing low Co: Cr are shown in blue.

4. CONCLUSIONS

It has been demonstrated that, within tissues associated with CoCrMo metal-on-metal hip replacements, elemental and chemical variability at the nanometric scale is observed. The distinctiveness of a XANES mapping approach is that it enables the entire chemical variability of an image field to be captured, as opposed to simply identifying which elements are present and measuring the speciation at single user defined points (reducing bias sampling). It is important to emphasise that a few point spectra with a broad (micron-sized) beam cannot represent the full chemical variability present within heterogeneous samples. In this case, a submicron level of detail with a mapping approach is an ideal interrogation method on such samples. In addition, small features (with sufficient intensity) have been interrogated yielding high-quality speciation information with a XANES mapping approach, which previously were difficult or impossible to record with conventional point XANES. Although this study highlights in particular, unreported heterogeneity in Cr speciation in peri-implant tissues associated with CoCrMo THRs, caution should be taken in over-interpretation of the findings with respect to correlations with clinical failures. Investigating the range of metallic chemistry that patients are exposed to is imperative to understand the underlying immunological response, to generate more appropriate biological models and to aid the understanding of device failure. However, the reported approach should now be used in conjunction with adequate patient sample sizes to allow generalization of findings.

CONTRIBUTIONS

O.A., A.P.M., R.A.M., H.F., H.C., J.E.P., and J.F.W.M. conceived the experiments and performed the measurements. All authors interpreted the data and drafted the manuscript. All authors revised the manuscript prior to submission.

FUNDED SOURCES

O.A. was funded by the National Institute for Health Research Award NIHR/CS/010/001. This article presents independent research funded by NIHR. The views expressed are those of the author(s) and not necessarily NIHR. A.P.M was supported by a Diamond Light Source Studentship. Additional funding is acknowledged: Natural Sciences and Engineering Research Council of Canada (grant No. 2017- 05862)

COMPETING INTERESTS

The authors declare no competing interests.

ACKNOWLEDGMENTS

The authors would like to thank Diamond Light Source (Beamlines, I18 and I14), the European Synchrotron Radiation Facility (Beamline ID21) and the Swiss Light Source (Beamline X05LA) for access to central facilities which produced the results shown here.

SUPPORTING INFORMATION

Co-location of Mo with high intensity Co and Cr identifies metallic features most closely matching the composition of the base metal (Supplementary Figure 1). Linear combination fitting (LCF) of metallic-CoCr and Cr(III) complexes, including Cr(OH)₃, Cr₂O₃ and CrPO₄ as standards (Supplementary Figure 2). The effects of X-ray resolution in identifying the Cr chemistry is shown (Supplementary Figure 3). Linear regression analysis identifies the range of post-edge variation between high-resolution XANES the average spectrum and a cross-correlation analysis between different data sets (Supplementary Figure 4). Semi-quantitative analysis of CoCr distributions (Supplementary Figure 5). Details of sequential energy points used for XANES mapping (Supplementary Table 1). A quantitative summary of Co and Cr within images recorded at I18 and ID21 is listed (Supplementary Table 2).

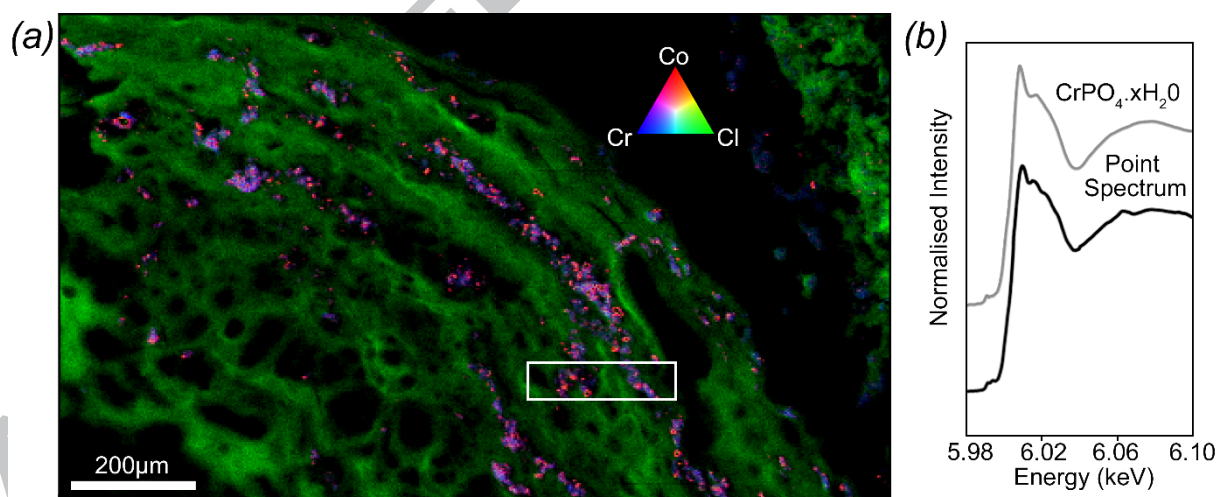
5. REFERENCES

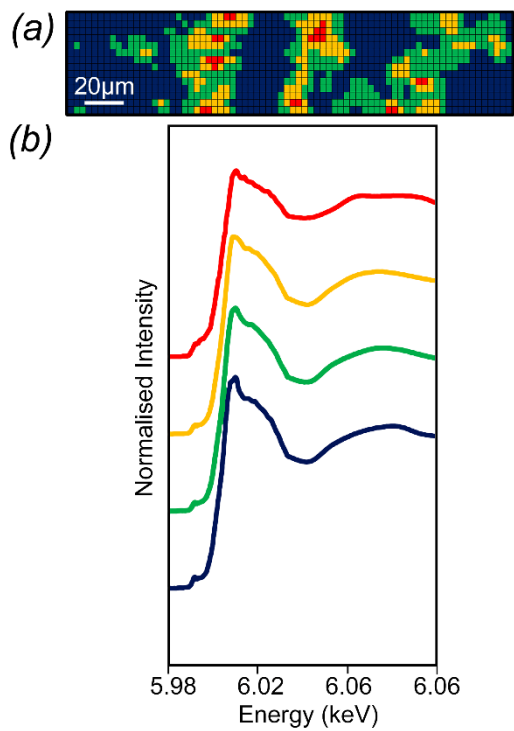
- [1] P. L. Drake, K. J. Hazelwood. Exposure-related health effects of silver and silver compounds: a review. *The Annals of occupational hygiene*. **2005**. 49, 575.
- [2] S. Bakand, A. Hayes, F. Dechsakulthorn. Nanoparticles: a review of particle toxicology following inhalation exposure. *Inhalation toxicology*. **2012**. 24, 125.
- [3] K.S. Smith, H. L. Huyck. An overview of the abundance, relative mobility, bioavailability, and human toxicity of metals. *The environmental geochemistry of mineral deposits*. **1999**. 6, 29.
- [4] G. Keegan, I. Learmonth, C. Case. Orthopaedic metals and their potential toxicity in the arthroplasty patient: a review of current knowledge and future strategies. *The Journal of bone and joint surgery. British volume*. **2007**. 89, 567.
- [5] I. Schreiver, B. Hesse, C. Seim, H. Castillo-Michel, J. Villanova, P. Laux, N. Dreiaek, R. Penning, R. Tucoulou, M. Cotte. Synchrotron-based v-XRF mapping and μ -FTIR microscopy enable to look into the fate and effects of tattoo pigments in human skin. *Scientific reports*. **2017**. 7, 11395.
- [6] X. Huang, P. K. Jain, I. H. El-Sayed, M. A. El-Sayed. Gold nanoparticles: interesting optical properties and recent applications in cancer diagnostics and therapy. *nanomedicine*. **2007**. 2, 681.
- [7] J.M. Christensen. Human exposure to toxic metals: factors influencing interpretation of biomonitoring results. *Science of the total environment*. **1995**. 166, 89.
- [8] I. Papageorgiou, C. Brown, R. Schins, S. Singh, R. Newson, S. Davis, J. Fisher, E. Ingham, C. Case. Human exposure to toxic metals: factors influencing interpretation of biomonitoring results. *Biomaterials*. **2007**. 28, 2946.
- [9] K. Midander, P. Cronholm, H. L. Karlsson, K. Elihn, L. Möller, C. Leygraf, I. O. Wallinder. Surface characteristics, copper release, and toxicity of nano- and micrometer-sized copper and copper (II) oxide particles: a cross-disciplinary study. *Small*. **2009**. 5, 389.
- [10] F. Billi, P. Benya, E. Ebramzadeh, P. Campbell, F. Chan, H. A. McKellop. Metal wear particles: What we know, what we do not know, and why. *International Journal of Spine Surgery*. **2009**. 3, 133.
- [11] D. F. Amanatullah, M. G. Sucher, G. F. Bonadurer, G. C. Pereira, M. J. Taunton. Metal in total hip arthroplasty: wear particles, biology, and diagnosis. *Orthopedics*. **2016**. 39, 371.
- [12] H. Yang, C. Liu, D. Yang, H. Zhang, Z. Xi. Comparative study of cytotoxicity, oxidative stress and genotoxicity induced by four typical nanomaterials: the role of particle size, shape and composition. *Journal of applied Toxicology*. **2009**. 29, 69.
- [13] M. Germain, A. Hatton, S. Williams, J. Matthews, M. Stone, J. Fisher, E. Ingham. Comparison of the cytotoxicity of clinically relevant cobalt–chromium and alumina ceramic wear particles in vitro. *Biomaterials*. **2003**. 24, 469.
- [14] A. M. El Badawy, R. G. Silva, B. Morris, K.G Scheckel, M.T. Suidan, T. M. Tolaymat. Surface charge-dependent toxicity of silver nanoparticles. *Environmental science & technology*. **2010**. 45, 283.
- [15] N. J Hallab, C. Vermes, C. Messina, K. A. Roebuck, T. T. Glant, J. J. Jacobs. Concentration- and composition-dependent effects of metal ions on human MG-63 osteoblasts. *Journal of Biomedical Materials Research*. **2002**. 60, 420.
- [16] T. Hanawa. Metal ion release from metal implants. *Materials Science & Engineering C*. **2004**. 24, 745.
- [17] I. D. Learmonth, C. Young, C. Rorabeck. The operation of the century: total hip replacement. *The Lancet*. **2007**. 370, 1508.
- [18] H. Waterson, M. Whitehouse, N. Greidanus, D. Garbuz, B. Masri, C. Duncan. Revision for adverse local tissue reaction following metal-on-polyethylene total hip arthroplasty is associated with a high risk of early major complications. *Bone Joint J*. **2018**. 100, 720.

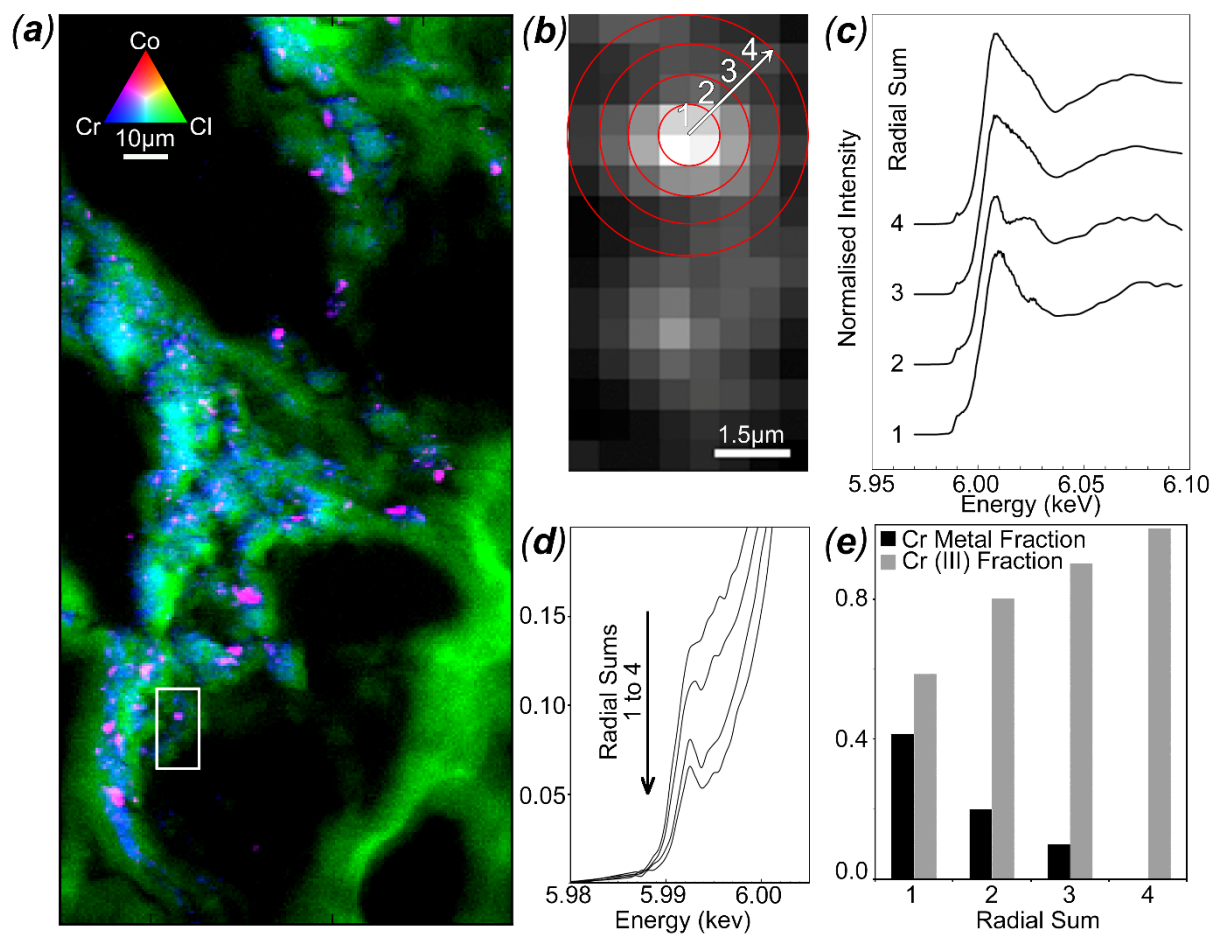
- [19] H. J. Cooper, C. J. Della Valle, R. A. Berger, M. Tetreault, W. G. Paprosky, M. S. Sporer, J. J. Jacobs. Corrosion at the head-neck taper as a cause for adverse local tissue reactions after total hip arthroplasty. *The Journal of bone and joint surgery. American volume*. **2012**. *94*, 1655.
- [20] B. J. McGrory, A. M. Payson, J. A. MacKenzie. Elevated intra-articular cobalt and chromium levels in mechanically assisted crevice corrosion in metal-on-polyethylene total hip arthroplasty. *The Journal of arthroplasty*. **2017**. *32*, 1654.
- [21] D. M. Templeton. Speciation in metal toxicity and metal-based therapeutics. *Toxics*. **2015**. *3*, 170.
- [22] *IARC Monographs on the Evaluation of Carcinogenic Risks to Humans*. **1990**. *49*, 49.
- [23] P. Apostoli, J. D. Cornelis, P. Hoet, D. Lison, D. Templeton, World Health Organization, Environmental Health Criteria, *234*. **2006**.
- [24] C. Uboldi, P. Urbán, D. Gilliland, E. Bajak, E. Valsami-Jones, J. Ponti, F. Rossi. Role of the crystalline form of titanium dioxide nanoparticles: Rutile, and not anatase, induces toxic effects in Balb/3T3 mouse fibroblasts. *Toxicology In Vitro*. **2016**. *31*, 137.
- [25] J. H. Kim, H. J. Gibb, P. D. Howe, World Health Organization, Concise International Chemical Assessment Document, *69*. **2006**.
- [26] C. Bresson, C. Darolles, A. Carmona, C. Gautier, N. Sage, S. Roudeau, R. Ortega, E. Ansoberlo, V. Malard. Cobalt chloride speciation, mechanisms of cytotoxicity on human pulmonary cells, and synergistic toxicity with zinc. *Metallomics*. **2013**. *5*, 133.
- [27] X.R Xia, N.A Monteiro-Riviere, S. Mathur, X. Song, L. Xiao, S. J. Oldenberg, B. Fadeel, J. E. Riviere. Mapping the surface adsorption forces of nanomaterials in biological systems. *ACS nano*. **2011**. *5*, 9074.
- [28] Z. Xia, B. F. Ricciardi, Z. Liu, X. von Ruhland, M. Ward, A. Lord, L. Hughes, S. R. Goldring, E. Purdue, D. Murray. Nano-analyses of wear particles from metal-on-metal and non-metal-on-metal dual modular neck hip arthroplasty. *Nanomedicine: Nanotechnology, Biology and Medicine*. **2017**. *13*, 1205.
- [29] S. Mittal, M. Revell, F. Barone, D. L. Hardie, G. S. Matharu, A. J. Davenport, R. A. Martin, M. Grant, F. Mosselmans, P. Pynsent. Lymphoid aggregates that resemble tertiary lymphoid organs define a specific pathological subset in metal-on-metal hip replacements. *PloS One*. **2013**. *8*, 63470.
- [30] Y. Z. Qin, J. A. Caruso, B. Lai, A. Matusch, J. S. Becker. Trace metal imaging with high spatial resolution: applications in biomedicine. *Metallomics*. **2011**. *3*, 28.
- [31] R. Lobinski, C. Moulin, R. Ortega. Imaging and speciation of trace elements in biological environment. *Biochimie*. **2006**. *88*, 1591.
- [32] R. Ortega, G. Deves, A. Carmona. Bio-metals imaging and speciation in cells using proton and synchrotron radiation X-ray microspectroscopy. *Journal of the Royal Society Interface*. **2009**. *6*, 649.
- [33] O. Addison, A. J. Davenport, R. J. Newport, S. Kalra, M. Monir, J. F. W. Mosselmans, D. Proops, R. A. Martin. Do 'passive' medical titanium surfaces deteriorate in service in the absence of wear?. *Journal of the Royal Society Interface*. **2012**. *9*, 3161.
- [34] M. Newville. Fundamentals of XAFS. *Reviews in Mineralogy and Geochemistry*. **2014**. *78*, 33.
- [35] A. J. Hart, P. D. Quinn, B. Sampson, A. Sandison, K. D. Atkinson, J. A. Skinner, J. J. Powell, J. F. W. Mosselmans. The chemical form of metallic debris in tissues surrounding metal-on-metal hips with unexplained failure. *Acta Biomaterialia*. **2010**. *6*, 4439.
- [36] A. J. Hart, P. D. Quinn, F. Lali, B. Sampson, J. A. Skinner, J. J. Powell, J. Nolan, K. Tucker, S. Donell, A. Flanagan, J. F. W. Mosselmans. Cobalt from metal-on-metal hip replacements may be the clinically relevant active agent responsible for periprosthetic tissue reactions. *Acta Biomaterialia*. **2012**. *8*, 3865.
- [37] H. A. Castillo-Michel, C. Larue, A. E. P. del Real, M. Cotte, G. Sarret. Practical review on the use of synchrotron based micro-and nano-X-ray fluorescence mapping and X-ray absorption

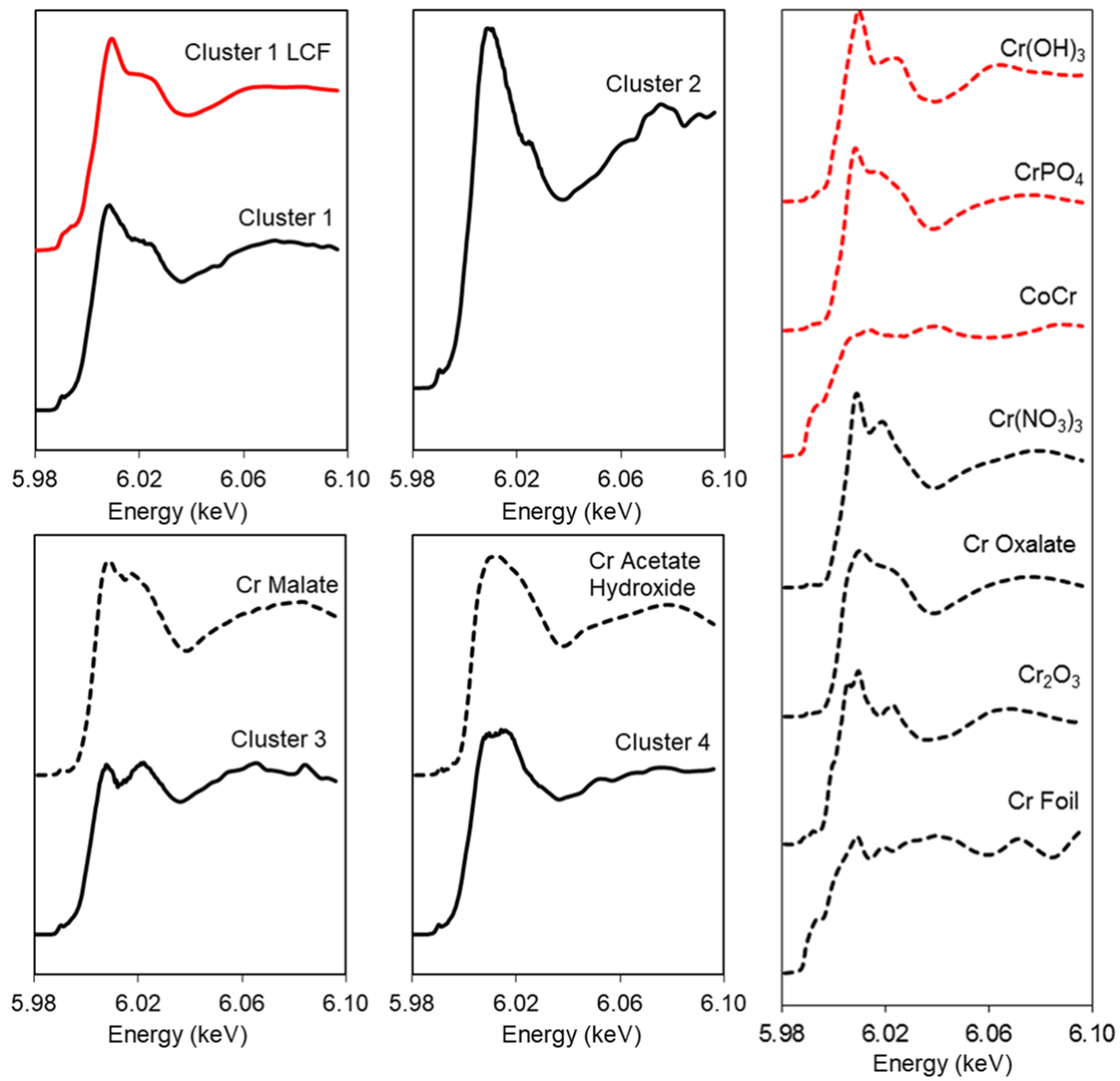
- spectroscopy to investigate the interactions between plants and engineered nanomaterials. *Plant Physiology and Biochemistry*. **2017**. 110, 13.
- [38] B. E. Etschmann, E. Donner, J. Brugger, D. L. Howard, M. D. de Jonge, D. Paterson, R. Naidu, K. G. Scheckel, C. G. Ryan, E. Lombi. Speciation mapping of environmental samples using XANES imaging. *Environmental Chemistry*. **2014**. 11, 341.
- [39] U. Boesenberg, C. G. Ryan, R. Kirkham, A. Jahn, A. Madsen, G. Moorhead, G. Falkenberg, J. Garrevoet. Fast XANES fluorescence imaging using a Maia detector. *Journal of Synchrotron Radiation*, **2018**. 25, 892.
- [40] M. M. L. da Cunha, S. Trepout, C. Messaoudi, T. D. Wu, R. Ortega, J. L. Guerquin-Kern, S. Marco. Overview of chemical imaging methods to address biological questions. *Micron*. **2016**. 84, 23.
- [41] J. L. Ong, M. R. Appleford, G. Mani, *Introduction to biomaterials: basic theory with engineering applications*. **2014**. Cambridge University Press.
- [42] P. J. Eng, M. Newville, M. L. Rivers, S. R. Sutton. Dynamically figured Kirkpatrick Baez X-ray microfocusing optics. *International Society for Optics and Photonics*. **1998**. 3449, 145.
- [43] J. F. W. Mosselmans, P. D. Quinn, A. J. Dent, S. A. Cavill, S. D. Moreno, A. Peach, P. J. Leicester, S.J Keylock, S. R. Gregory, K. D. Atkinson, J. R. Rosell. I18—the microfocus spectroscopy beamline at the Diamond Light Source. *Journal of Synchrotron Radiation*. **2009**. 16, 818.
- [44] M. Salomé, M. Cotte, R. Baker, R. Barrett, N. Benseny-Cases, G. Berruyer, D. Bugnazet, H. Castillo-Michel, C. Cornu, B. Fayard. The ID21 scanning X-ray microscope at ESRF. *Journal of Physics: Conference Series IOP Publishing*. **2013**. 425, 182004.
- [45] V. A. Sole, E. Papillon, M. Cotte, P. Walter, J. Susini. A multiplatform code for the analysis of energy-dispersive X-ray fluorescence spectra. *Spectrochimica Acta Part B-Atomic Spectroscopy*. **2007**. 62, 63.
- [46] M. D. Bethesda. ICRU Reports. *International Commission on Radiation Units and Measurements*. **1989**. 44, 35.
- [47] M. Lerotic, R. Mak, S. Wirick, F. Meirer, C. Jacobsen. MANTiS: a program for the analysis of X-ray spectromicroscopy data. *J. Synchrotron Rad*. **2014**. 21, 1206.
- [48] K. Marstal, F. Berendsen, M. Staring, S. Klein. SimpleElastix: A user-friendly, multi-lingual library for medical image registration. *Proceedings of the IEEE Conference on Computer Vision and Pattern Recognition Workshops*. **2016**. 134.
- [49] B. Ravel, M. Newville. ATHENA, ARTEMIS, HEPHAESTUS: data analysis for X-ray absorption spectroscopy using IFEFFIT. *Journal of Synchrotron Radiation*. **2005**. 12, 537.
- [50] A. E. Goode, J. M. Perkins, A. Sandison, C. Karunakaran, H. K. Cheng, D. Wall, J. A. Skinner, A. J. Hart, A. E. Porter, D. W. McComb, M. P. Ryan. Chemical speciation of nanoparticles surrounding metal-on-metal hips. *Chemical Communications*. **2012**. 48, 8335
- [51] N. Mölders, P. J. Schilling, J. Wong, J.W. Roos, I. L. Smith. X-ray fluorescence mapping and micro-XANES spectroscopic characterization of exhaust particulates emitted from auto engines burning MMT-added gasoline. *Environmental science & technology*. **2001**. 35, 3122.
- [52] P. Quinn, J. Parker, F. Cacho-Nerin, M. Walker, P. Howes. The Hard X-ray Nanoprobe Beamline at Diamond-Current Status. *Microscopy and Microanalysis*. **2018**. 24, 244.
- [53] A. J. Hart, A. Sandison, P. Quinn, B. Sampson, K. D. Atkinson, J. A. Skinner, A. Goode, J. J. Powell, J. F. W. Mosselmans. Microfocus study of metal distribution and speciation in tissue extracted from revised metal on metal hip implants. *Journal of Physics: Conference Series*. **2009**. 1, 12208.
- [54] B. Kanngiesser. Quantification procedures in micro X-ray fluorescence analysis. *Spectrochimica Acta Part B-Atomic Spectroscopy*. **2003**. 58, 609.
- [55] B. Bewer. Quantification estimate methods for synchrotron radiation X-ray fluorescence spectroscopy. *Nuclear Instruments & Methods in Physics Research Section B-Beam Interactions with Materials and Atoms*. **2015**. 347, 1.
- [56] R. Sitko, B. Zawisza. X-ray Spectroscopy. *InTech*. **2012**.

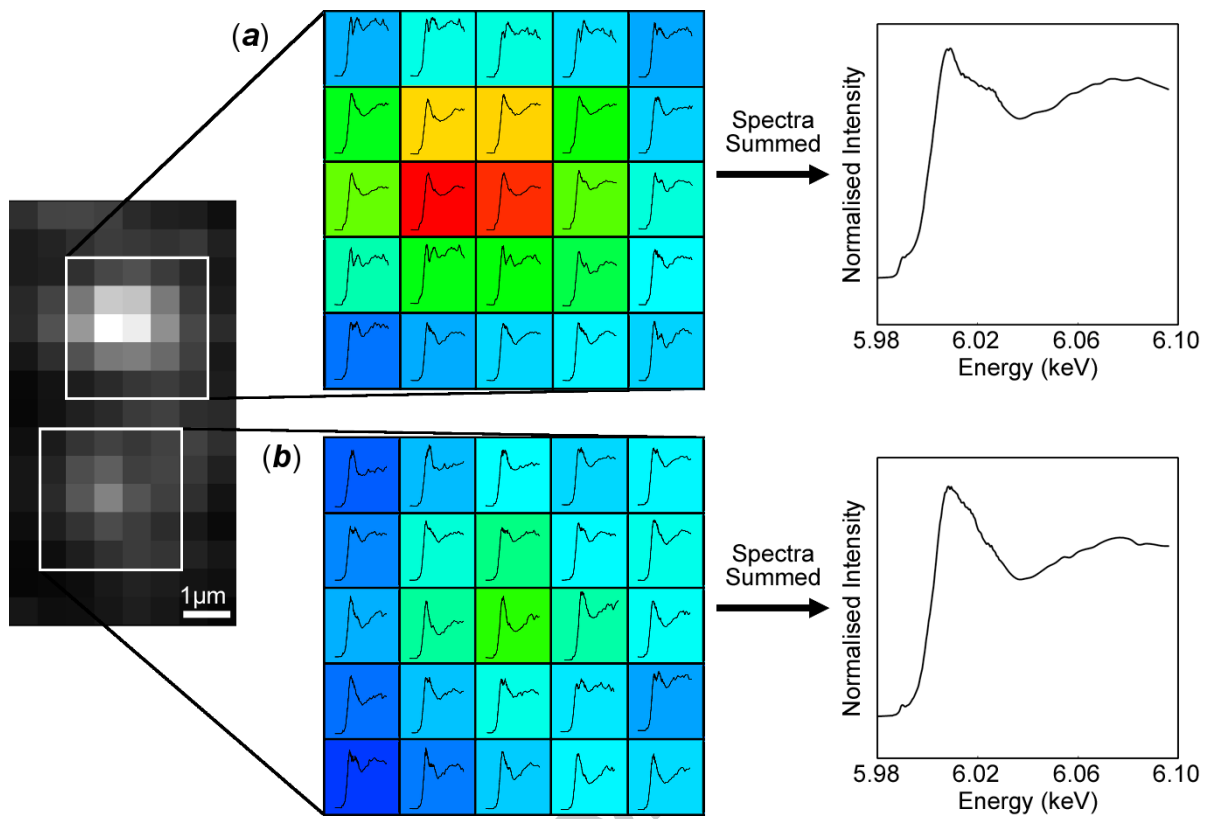
- [57] R. M. Rousseau, J. A. Boivin. The fundamental algorithm: a natural extension of the Sherman equation, part I: theory. *Rigaku J.* **1998.** 15, 13.
- [58] T. Schoonjans, V. A. Sole, L. Vincze, M. Sanchez del Rio, K. Appel, C. Ferrero. A general Monte Carlo simulation of energy-dispersive X-ray fluorescence spectrometers—Part 6. Quantification through iterative simulations. *Spectrochimica Acta Part B.* **2013.** 82, 36.
- [59] I. Swiatkowska, J. F. W. Mosselmans, T. Geraki, C. C. Wyles, J. J. Maleszewski, J. Henckel, B. Sampson, D. B. Potter, I. Osman, R. T. Trousdale. Synchrotron analysis of human organ tissue exposed to implant material. *Journal of Trace Elements in Medicine and Biology.* **2018.** 46, 128.
- [60] M. A. Koronfel, A. E. Goode, J. N. Weker, S. E. Tay, C. A. Stitt, T. A. Simoes, J. F. W. Mosselmans, P. Quinn, R. Brydson, A. Hart. Understanding the reactivity of CoCrMo-implant wear particles. *npj Materials Degradation.* **2018.** 2, 8.
- [61] B. Sampson, A. Hart. Clinical usefulness of blood metal measurements to assess the failure of metal-on-metal hip implants. *Annals of Clinical Biochemistry.* **2012.** 49, 118.
- [62] B. D. Kerger, R. Gerads, H. Gurleyuk, A. Urban, D. J. Paustenbach. Total cobalt determination in human blood and synovial fluid using inductively coupled plasma-mass spectrometry: method validation and evaluation of performance variables affecting metal hip implant patient samples. *Toxicological & Environmental Chemistry.* **2015.** 97, 1145.
- [63] H. Lin, J. D. Bumgardner. Changes in the surface oxide composition of Co–Cr–Mo implant alloy by macrophage cells and their released reactive chemical species. *Biomaterials.* **2004.** 25, 1233.
- [64] M. Jenko, M. Gorenssek, M. Godec, M. Hodnik, B. S. Batic, C. Donik, J. T. Grant, D. Dolinar. Surface chemistry and microstructure of metallic biomaterials for hip and knee endoprostheses. *Applied Surface Science.* **2018.** 427, 584.











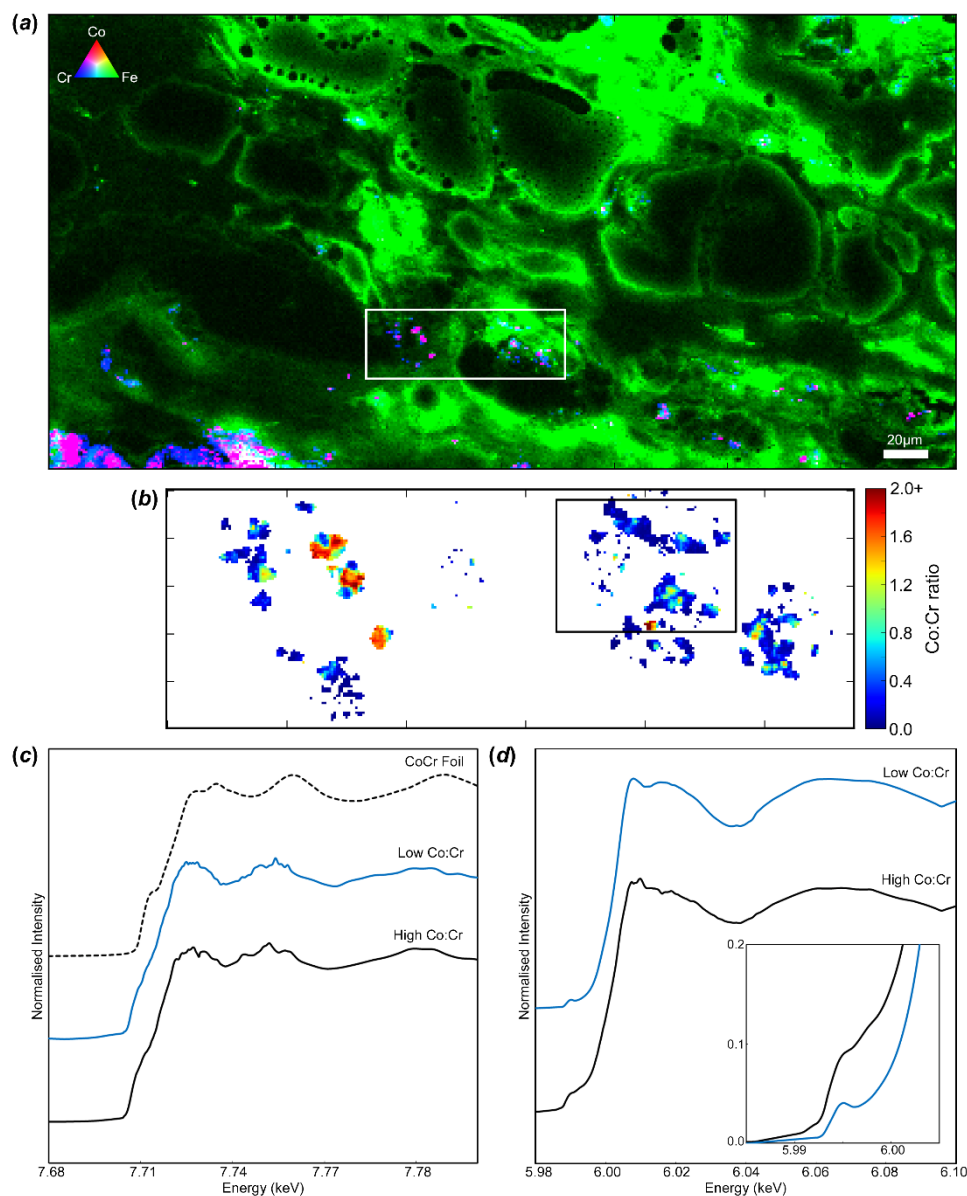


Figure 1. μ XRF and μ XANES analysis was undertaken at I18, *Diamond Light Source, UK*. (a) shows an XRF map of *ex-vivo* synovial sheath tissue, Cl (green) is a typical tissue marker and shows the geometry. Co and Cr (red and blue respectively) are co-located in areas but Cr appears more abundantly and in diffuse regions as well as single features. A point XANES measurement is shown in (b) which utilized a 3 μ m beam on a region with high Cr signal. The spectrum shows close resemblance to CrPO_4 (also shown in b).

Figure 2. A 3 μ m resolution beam was utilized to generate a $\sim 250 \times 50 \mu\text{m}$ XANES map. Each point was grouped based on spectral similarities into four clusters. The resulting cluster map is shown in (a). The resulting spectra are shown in (b).

Figure 3. sub-micron-XRF and XANES mapping analysis undertaken on ID21. (a) shows a high resolution XRF map on the *ex-vivo* soft tissue (600 nm beam size). At this resolution it is more evident

that CoCr features are present within a network of diffuse Cr. **(b)** shows an intensity map of the area subjected to Cr XANES mapping, highlighted by an inset in **(a)**. To understand speciation variation across the high intensity CoCr regions, radial selections of the XANES spectra were taken, starting in the middle and moving outwards, the results are shown in **(c)**. The pre-edge region, highlighted in **(d)**, shows the further away from the centre of the feature causes a reduction in metallic fraction. **(e)** shows a histogram of how the metallic fraction reduces when moving away from the inside the core outwards (based off the pre-edge peak).

Figure 4. Shows the cluster analysis of the XANES mapping data in the region identified in Figure 3. XANES data was stacked and aligned using in-house ID21 algorithms. Six principle components were identified but only 4 clusters were used as after this point the spectra could be reproduced using linear combinations of standards in different ratios. Each cluster is shown on a separate graph (solid black line) and Cr standards which are thought to contribute to the spectra are shown (dashed-line). Cluster 1 is the most abundant spectra and from the linear combination fitting (LCF) it is likely to be a combination of CrPO_4 , $\text{Cr}(\text{OH})_3$ and CoCr (34%, 41% and 25%, respectively). The spectrum in Cluster 2 contains a unique feature present at ~ 6025 eV which is not present in any of the organic or inorganic reference spectra. Cluster 3 and 4 are combinations of Cr complexes with CoCr, however a LCF is not shown as the predominate species present is Cr malate and acetate hydroxide, respectively.

Figure 5. The two spectra shown on the right-hand side are a result of summing a $3 \times 3 \mu\text{m}$ area from the XANES map, mimicking a lower resolution static measurement. By averaging over a larger area some spectral features are lost which may be essential for working out which species are present. The top region results in a spectrum with prominent features similar to $\text{Cr}(\text{OH})_3$ and CrPO_4 complexes. The bottom region spectrum has a broader peak with no secondary peak, this feature is similar to those shown by organic Cr complexes.

Figure 6. **(a)** XRF map of *ex-vivo* soft tissues recorded at the hard X-ray nano-probe I14. A step of $1 \mu\text{m}$ was used both horizontally and vertically. The elements shown are Co (red), Cr (blue) and Fe (green). Fe was utilised to observe the tissue geometry as it contained the highest signal-to-noise of all the soft tissue elements present. **(b)** Co: Cr ratio map from area highlighted in Figure 6a, a resolution of 250 nm was used. **(c)** and **(d)** XANES spectra from the XANES map region highlighted in Figure 6b. The spectra shown are a result of summing spectra based on their Co: Cr ratios. Spectra containing high Co: Cr are shown in black, whereas spectra containing low Co: Cr are shown in blue.

Supplementary Figure 1. A matching tissue section was subsequently imaged at the Swiss Light Source (SLS) at the Paul Scherrer Institute (*Villigen, Switzerland*). A resolution of $1 \mu\text{m}$ was used at the MicroXAS beamline with a 20.2 keV X-ray energy to detect Mo. An acquisition time of 1 s per point was used to generate two maps in different locations (a high Co region and high Cr region). Molybdenum was found in all cases and showed a high correlation with Co **(a)** and Cr **(b)**.

Supplementary Figure 2. Linear combination fittings for the radial selections shown in Figure 3c (1-4 left to right). Data and their respective fits are shown as the black and red traces respectively. Software package ATHENA was used to generate the LCF on normalized spectra. The fit was limited to 15 eV below and 21 eV above the absorption edge and the E_0 of the standards was kept constant. CrCo was used as the metallic portion with CrPO_4 , $\text{Cr}(\text{OH})_3$, Cr_2O_3 and Cr acetate hydroxide as the Cr complex. The fit on radial selection 2 deviates from the data more than the other selections. This was due to a number of spectra within the selection containing unique spectral features which could not be reproduced with the Cr standards available.

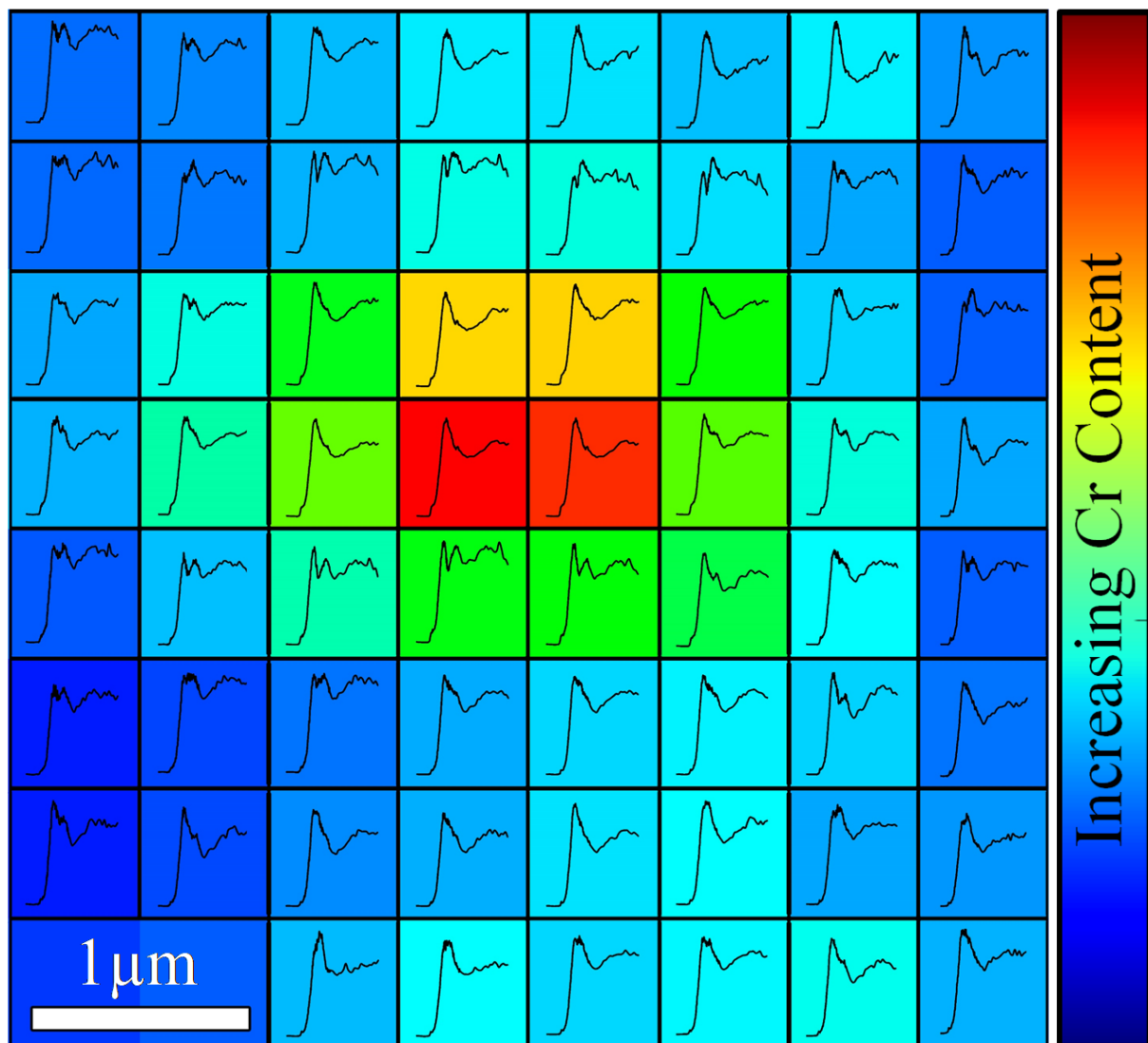
Supplementary Figure 3. Illustration of the spectral variation observed in Figure 5a. The spectra generated through XANES mapping were grouped based on post-edge similarities. Six groups indicative of the variation in Cr speciation are compared with the average spectrum of the 3 x 3 μm measurement area (25-pixel average) and demonstrates that a reduced resolution measurement under-estimates the range of Cr species present within these *ex-vivo* tissues.

Supplementary Figure 4. (a) Linear regression analysis was applied to the post-edge region (6.00 – 6.04 keV) on the high-resolution XANES map data and is compared with the 25-pixel average in Figure 5a. This energy domain was selected as typically variation here indicates differences in Cr(III) speciation. The R^2 values are shown and in all cases $p < 0.05$. Only half of the spectra observed are well-represented by the 3x3 μm^2 average ($R^2 > 0.9$) **(b)** Linear regression analysis was used to cross-correlate XANES spectra acquired using different measurement approaches (point spectra vs mapping at different spatial resolutions). For equivalent measurement areas (3x3 μm^2) the 25-pixel average (equivalent area), measured at ID21 correlated strongly ($R^2=0.986$) with the 3x3 μm point XANES measured at I18 **(A)**. Both of which have high correlative values with a CrPO_4 standard **(B)** which is the most frequently reported Cr species in tissues associated with THR systems. Whilst XANES mapping at a 3 μm resolution (Figure 2) showed variation in the spectra identified by PCA, linear regression comparing the most different components (cluster 1 **(C)** and 4 **(D)**) fails to discriminate significant differences. As over 1400 spectra were analysed in the I18 XANES map alone and insignificant variation was observed, this emphasises that the resolution is limiting factor in the characterisation of Cr speciation in these samples.

Supplementary Figure 5. (a) and **(b)** are ratio maps (250 nm resolution) from an area within Figure 6a. The analysis of **(a)** has been treated qualitatively, using only the number of counts to determine the ratios. Whereas the analysis of **(b)** has been considered semi-quantitatively considering the differences in attenuation of Co and Cr due to the different wavelengths. Both **(a)** and **(b)** are plotted using the same colour scale to allow direct comparison. **(c)** shows the resulting ratio distribution in a histogram, the blue plot represents the qualitative analysis **(a)**, the red plot represents the semi-quantitative analysis **(b)**. It is clear from these results the Co: Cr ratios are significantly lower when analysing semi-quantitatively, which are deemed more accurate.

SIGNIFICANCE

Metal implants are routinely used in healthcare but may fail following degradation in the body. Although specific implants can be identified as ‘high-risk’, our analysis of failures is limited by a lack of understanding of the chemistry of implant metals within the peri-prosthetic milieu. A new approach to identify the speciation and variability in speciation at sub-micron resolution, of dilute exogenous metals within biological tissues is reported; applied to understanding the failure of metallic (CoCrMo) total-hip-replacements widely used in orthopedic surgery. Much greater variation in Cr chemistry was observed compared with previous reports and included phosphate, hydroxide, oxide, metal and organic complexes. This variability may explain lack of agreement between biological responses observed in experimental exposure models and clinical outcomes.



ACCEPTED